

REPORT DOCUMENTATION PAGE

Form Approved
OMB No. 0704-0188

Public reporting burden for this collection of information is estimated to average 1 hour per response, including the time for reviewing instructions, searching existing data sources, gathering and maintaining the data needed, and completing and reviewing this collection of information. Send comments regarding this burden estimate or any other aspect of this collection of information, including suggestions for reducing this burden to Department of Defense, Washington Headquarters Services, Directorate for Information Operations and Reports (0704-0188), 1215 Jefferson Davis Highway, Suite 1204, Arlington, VA 22202-4302. Respondents should be aware that notwithstanding any other provision of law, no person shall be subject to any penalty for failing to comply with a collection of information if it does not display a currently valid OMB control number. PLEASE DO NOT RETURN YOUR FORM TO THE ABOVE ADDRESS.

1. REPORT DATE (DD-MM-YYYY)		2. REPORT TYPE Technical Papers		3. DATES COVERED (From - To)	
4. TITLE AND SUBTITLE				5a. CONTRACT NUMBER	
				5b. GRANT NUMBER	
				5c. PROGRAM ELEMENT NUMBER	
6. AUTHOR(S)				5d. PROJECT NUMBER 2303	
				5e. TASK NUMBER m2c8	
				5f. WORK UNIT NUMBER	
7. PERFORMING ORGANIZATION NAME(S) AND ADDRESS(ES)				8. PERFORMING ORGANIZATION REPORT	
Air Force Research Laboratory (AFMC) AFRL/PRS 5 Pollux Drive Edwards AFB CA 93524-7048					
9. SPONSORING / MONITORING AGENCY NAME(S) AND ADDRESS(ES)				10. SPONSOR/MONITOR'S ACRONYM(S)	
Air Force Research Laboratory (AFMC) AFRL/PRS 5 Pollux Drive Edwards AFB CA 93524-7048				11. SPONSOR/MONITOR'S NUMBER(S)	
12. DISTRIBUTION / AVAILABILITY STATEMENT					
Approved for public release; distribution unlimited.					
13. SUPPLEMENTARY NOTES					
14. ABSTRACT					
15. SUBJECT TERMS					
16. SECURITY CLASSIFICATION OF:			17. LIMITATION OF ABSTRACT	18. NUMBER OF PAGES	19a. NAME OF RESPONSIBLE PERSON Leilani Richardson
a. REPORT Unclassified	b. ABSTRACT Unclassified	c. THIS PAGE Unclassified	A		19b. TELEPHONE NUMBER (include area code) (661) 275-5015

62

Separate items are enclosed

TP-FY99-0090

C8

Spreadsheet
 PTS

In-House
NDUM FOR PRR (Contractor Publication)

As: PROI (TI) (STINFO)

4 May 1999

JECT: Authorization for Release of Technical Information, Control Number: AFRL-PR-ED-TP-FY99-0090
Tam and Fajardo, et. al. "High Resolution Infrared Absorption Spectra of Methane Molecules Isolated in Solid
Parahydrogen Matrices"

For submission to the Journal of Chemical Physics

(Public Release)

High Resolution Infrared Absorption Spectra of Methane Molecules Isolated in Solid Parahydrogen Matrices

Simon Tam and Mario E. Fajardo^{a)}

Propulsion Directorate, US Air Force Research Laboratory
AFRL/PRSP, Bldg. 8451, Edwards AFB, CA 93524-7680

and

Hiroyuki Katsuki, Hiromichi Hoshina, and Takamasa Momose^{b)}

Department of Chemistry, Graduate School of Science, Kyoto University,
and Japan Science and Technology Corporation (JST),
Kyoto 606-8502, Japan

a) email: Mario_Fajardo@ple.af.mil

b) email: momose@kuchem.kyoto-u.ac.jp

Submitted to J. Chem. Phys. _____, Received _____, Accepted _____

ABSTRACT

We present high resolution ($\sim 0.01 \text{ cm}^{-1}$) infrared absorption spectra of the ν_4 band of methane doped parahydrogen (CH_4/pH_2) solids produced by two different techniques: gas condensation in an enclosed cell at $T \approx 8 \text{ K}$, and rapid vapor deposition onto a $T \approx 2 \text{ K}$ substrate in vacuum. The spectrum of the rapid vapor deposited solid contains a novel progression of single peaks with $\approx 5 \text{ cm}^{-1}$ spacing, superimposed over the known spectrum of CH_4 molecules trapped in sites of D_{3h} symmetry in hexagonal close-packed (hcp) solid pH_2 . New theoretical calculations of the rovibrational transitions of a tetrahedral molecule in an external field of O_h symmetry permit the assignment of this new progression to CH_4 molecules trapped in crystalline face centered cubic (fcc) regions of the pH_2 solid. Annealing of the rapid vapor deposited samples to $T \approx 5 \text{ K}$ decreases the intensities of the $\text{CH}_4/\text{pH}_2(\text{fcc})$ absorptions, and results in intensity changes for parallel and perpendicularly polarized $\text{CH}_4/\text{pH}_2(\text{hcp})$ transitions. We discuss these phenomena, and the narrow (0.01 to 0.04 cm^{-1} FWHM) absorption linewidths, in terms of the microscopic structure of the pH_2 hosts.

20021121 037

Approved for public release; distribution unlimited

I. INTRODUCTION

Since the discovery in the late 1980's by Oka and coworkers¹ of astonishingly sharp infrared (IR) absorption lines in doped cryogenic parahydrogen (pH₂) solids, the popularity of pH₂ as a host for matrix isolation spectroscopy (MIS) has grown steadily. The favorable properties of pH₂ as a matrix host have been discussed at length,¹⁻⁶ and summarized quite recently,³ so we will not re-enumerate them here. Rather, we focus our attention more narrowly onto issues arising from the comparison of MIS experiments performed on pH₂ solids prepared in different laboratories.

Liquid pH₂ crystallizes into a hexagonal close-packed (hcp) solid upon slow cooling below T = 13.8 K; however, this process cannot generally be used to prepare doped solids. Two principal methods for producing thick, transparent, doped pH₂ solids have emerged: gas condensation in an enclosed cell^{2,3} held at T ≈ 8 K, and rapid vapor deposition^{5,6} onto a much colder substrate in vacuum. Since these solids can be produced under highly non-equilibrium conditions they might contain a variety of metastable microscopic structures,⁷ suggesting a corresponding variety of perturbations to the spectroscopy of dopant molecules. This manuscript addresses this connection between the observed rovibrational spectroscopy of dopant molecules and the microscopic structure of the pH₂ host for the specific case of methane doped parahydrogen (CH₄/pH₂) solids.

IR absorption spectra of CH₄/pH₂ solids produced by gas condensation in an enclosed cell at T ≈ 8 K have been previously reported.⁸⁻¹⁰ Detailed analysis shows the existence of quantized CH₄ rotational states, with all spectral features consistent with trapping of CH₄ molecules in sites of *D_{3h}* symmetry (a variety of linear and non-linear spectroscopies have demonstrated that pure

pH₂ solids grown in like manner are polycrystalline aggregates of the thermodynamically stable hcp phase¹). Thus, these experimental and theoretical results provide a well understood benchmark against which to measure IR data obtained from other CH₄/pH₂ samples.

Rapid vapor deposition of pre-cooled pH₂ gas onto a \approx 2 K substrate in vacuum can produce millimeters thick, optically transparent pH₂ solids.⁵ Such samples can be doped readily by any conventional MIS dopant introduction technique, and anecdotal evidence suggests that the lower condensation temperatures result in improved dopant isolation efficiency over the enclosed cell method. However, the lower condensation temperatures also promote the formation of metastable solid structures, raising the specter of multiple trapping sites and attendant inhomogeneous spectral perturbations. IR and Raman spectra of pure pH₂ solids formed by rapid vapor deposition show that these samples: (a) are not amorphous, (b) are not porous, but (c) do contain some non-hcp regions.⁵ The Raman data indicate that the non-hcp regions are most likely face-centered cubic (fcc),^{5,7} which differs from hcp in the stacking arrangement of close-packed planes.¹¹

In what follows, we explore the impact of these non-hcp solid pH₂ regions on the spectroscopy of trapped CH₄ molecules. We extend the theory of the rovibrational states of a tetrahedral molecule in a field of D_{3h} symmetry⁸ (e.g., CH₄ in hcp pH₂) to encompass a tetrahedral molecule in an octahedral (O_h) external field (e.g., CH₄ in fcc pH₂). We show that the details of the ν_4 absorption band of rapid vapor deposited CH₄/pH₂ samples can be explained as a superposition of spectra for CH₄ trapped in both hcp and fcc regions.

This new understanding of dopant molecule spectroscopy in return provides a practical diagnostic of the microscopic structures present in solid pH₂ samples produced under variable

conditions. We hope the methodology developed during the present collaboration will facilitate the comparison of MIS results obtained from doped pH₂ solids produced in other laboratories.

II. THEORY

A. fcc Crystal Field and Symmetry Classification

We have already developed the theory for the analysis of the rovibrational transitions of methane in an hcp crystal⁸ based on the extended group theory.¹² The same theoretical framework can be applied to the system of methane in an fcc crystal, but a modification is necessary to take into account the different symmetries between the hcp and fcc crystal structures. In this section we consider a methane molecule occupying a single substitutional site of an fcc crystal of parahydrogen.

The structure of a single substitutional vacancy in an fcc crystal belongs to a point group of O_h , composed of 48 symmetry operations, while the feasible permutation-inversion group of methane is G_{24} , which is isomorphic to a point group of T_d , composed of 24 elements. The appropriate extended group G^{fcc} for methane in an fcc crystal can be obtained by considering the parity of the whole system properly. The extended group G^{fcc} thus composed is isomorphic to the direct product group of the O and T_d point groups. The irreducible representation of the group G^{fcc} is labeled as $\Gamma\bar{\Gamma}'$ where Γ is a representation of the point group O , and Γ' is that of the group G_{24} (T_d). The extended group for a tetrahedral molecule in an O_h field is given in detail by King and Horning.¹³

The symmetry adapted rotational wavefunctions in terms of the extended group G^{fcc} are obtained by considering the transformation of the symmetric top rotational wavefunction $|kjm\rangle$

under each operation of the extended group. The symmetry adapted wavefunctions for $J=0, 1$, and 2 in the ground vibrational state are listed in Table 1. Here, the symmetric top rotational wavefunction is defined as $|kJm\rangle = [2J+1/8\pi^2]^{1/2} D_{k,m}^{(J)}(\{\chi\theta\varphi\})$ where the phase of Wigner's rotation matrix $D_{k,m}^{(J)}$ is the same as before.^{8,14} We define the crystal axis such that hydrogen molecules occupy the lattice points located at $\mathbf{R}_i = l_1\mathbf{a}_1 + l_2\mathbf{a}_2 + l_3\mathbf{a}_3$ where $\mathbf{a}_1 = a(\mathbf{i} + \mathbf{j})$, $\mathbf{a}_2 = a(\mathbf{j} + \mathbf{k})$, and $\mathbf{a}_3 = a(\mathbf{k} + \mathbf{i})$ are the primitive vectors with the unit vectors $\mathbf{i}, \mathbf{j}, \mathbf{k}$ along the crystal x, y, z -axes. The coefficient a is related to the nearest neighbor distance R_0 as $a = R_0/\sqrt{2}$, and $l_i = 0, \pm 1, \pm 2, \dots$ are the cell indices. To define the molecule-fixed axis of methane, one of the C_2 symmetry axes of methane is taken as the z -axis and the other two are taken as the x and y axes, so that one of the C_3 axes is oriented to point in the $(1, 1, 1)$ direction of the molecule-fixed axis.

In order to analyze the rovibrational states of methane interacting with parahydrogen, we need to consider the interaction which depends only on the orientation of methane. The interaction potential for a methane in an fcc crystal has to be invariant under any symmetry operation of the extended group G^{fcc} . Thus, the functional form of the potential can be obtained directly from the group theory. The first anisotropic potential is found to be

$$V(\Omega) = \varepsilon_4^{fcc} \frac{1}{24} \left[\sqrt{70} \{D_{4,0}^{(4)}(\Omega) + D_{0,4}^{(4)}(\Omega) + D_{-4,0}^{(4)}(\Omega) + D_{0,-4}^{(4)}(\Omega)\} \right. \\ \left. + 14D_{0,0}^{(4)}(\Omega) + 5 \{D_{4,4}^{(4)}(\Omega) + D_{-4,4}^{(4)}(\Omega) + D_{4,-4}^{(4)}(\Omega) + D_{-4,-4}^{(4)}(\Omega)\} \right] \quad (1)$$

where Ω is the orientation of methane relative to the z -axis of the crystal. Note that the functional form of the potential in Eq. (1) depends on the definition of the crystal and molecule axes.¹⁵

As is seen in Eq. (1), the first anisotropic interaction of methane in an fcc crystal is expressed in terms of the fourth order rotation matrix. On the other hand, the lowest order anisotropic interaction potential in an hcp crystal is found to be expressed by the third order matrix.⁸ The difference comes from the different symmetry between two crystal structures: the fcc lattice is higher in symmetry than the hcp lattice.

The difference is more easily understood by constructing the interaction potential from all the pairwise intermolecular interactions between the methane and hydrogen molecules in a crystal. The first two symmetry adapted interaction functions for a single pair of a methane and a hydrogen molecule are given as:

$$v_3(R, \omega) = a_3(R) \frac{i}{\sqrt{2}} [D_{2,0}^{(3)}(\omega) - D_{-2,0}^{(3)}(\omega)] \quad (2)$$

and

$$v_4(R, \omega) = a_4(R) \frac{1}{2\sqrt{6}} [\sqrt{5} \{D_{4,0}^{(4)}(\omega) + D_{-4,0}^{(4)}(\omega)\} + \sqrt{14} D_{0,0}^{(4)}(\omega)] \quad (3)$$

where R is the distance between the methane and hydrogen molecules and ω is the orientation of methane relative to the pair axis between the two molecules. The symbols $a_3(R)$ and $a_4(R)$ are the distance dependent coefficients for these interactions. The pairwise potentials in Eqs. (2) and (3) are more concisely written as:

$$v_l(R, \omega) = a_l(R) \sum_{k=-l}^l A_k^l D_{k,0}^{(l)}(\omega) \quad (4)$$

where $l=3, 4$ and A_k^l is a proper coefficient, *i.e.* $A_{\pm 2}^3 = \pm i/\sqrt{2}$, $A_{\pm 4}^4 = \sqrt{30}/12$, and $A_0^4 = \sqrt{21}/6$.

Since the interaction between methane and parahydrogen is mainly due to the dispersion force which is nearly additive, the interaction potential in the crystal can be obtained as a summation

of pairwise intermolecular interactions of Eqs. (2) and (3). Using the fact that the coefficients $a_3(R)$ and $a_4(R)$ for the dispersion interaction are proportional to R^{-7} and R^{-8} , respectively,¹⁶ the l -th order interaction potential in the crystal $V_l(\Omega)$ is expressed as:

$$V_l(\Omega) = a_l(R_0) \sum_{m=-l}^l S_{\delta,m}^{(l)} \sum_{k=-l}^l A_k^l D_{k,m}^{(l)}(\Omega) \quad (5).$$

Here, the symbol $S_{\delta,m}^{(l)}$ is a crystal sum defined as:

$$S_{\delta,m}^{(l)} = \sum_{j=2}^{\infty} \left(R_0 / R_j \right)^{\delta} D_{0,m}^{(l)} * (\Omega_{1 \rightarrow j}) \quad (6)$$

where $\delta=7$ for $l=3$ and $\delta=8$ for $l=4$, R_0 is the nearest neighbor distance, R_j is the distance between the methane and the j -th hydrogen molecule, and the angle $\Omega_{1 \rightarrow j}$ is the orientation of the pair axis between the methane and the j -th hydrogen molecule relative to the crystal axis. Note that the crystal sum $S_{\delta,m}^{(l)}$ depends only on the configuration of the molecules in the lattice.

In the case of an hcp crystal the crystal sum for $l=3$, $m=\pm 3$ is not zero, and thus the third order potential caused by the pairwise interaction of Eq. (2) remains (see Eq. (17) in Ref. 8). On the contrary, in the case of an fcc crystal, the first non-vanishing crystal sum is that of $l=4$ ($m=0, \pm 4$), namely, $S_{8,0}^{(4)} = \mp \sqrt{14/5} S_{8,\pm 4}^{(4)} = -1.5729$. Thus, the third order potential does not exist in this case but the fourth order potential resulting from the interaction of Eq. (3) remains with the functional form given in Eq. (1).

B. Order Estimation

Since the potential in an fcc crystal is a function of the fourth order Wigner's matrix, the splittings of rotational M sublevels are expected to be small compared with that in hcp crystal.

The coefficient ε_4^{fcc} in Eq. (1) is related to the coefficient a_4 in Eq. (3) as:

$$\varepsilon_4^{fcc} = 6S_{8,0}^{(4)}a_4(R_0)/\sqrt{21} \quad (7).$$

By use of the relation¹⁵

$$a_4(R) = \frac{3\sqrt{35}}{28} \frac{\Delta C_{CH_4}}{A_{CH_4}} \frac{1}{R} a_3(R) \quad (8)$$

we obtain the following equation relating the coefficient ε_4^{fcc} in Eq. (1) and the coefficient ε_{3c}^{hcp} of the crystal field in an hcp crystal defined in our previous paper,⁸

$$\varepsilon_4^{fcc} = \frac{3\sqrt{30}}{28i} \frac{S_{8,0}^{(4)fcc}}{S_{7,3}^{(3)hcp}} \frac{\Delta C_{CH_4}}{A_{CH_4}} \frac{1}{R_0} \varepsilon_{3c}^{hcp} \quad (9).$$

Here, $S_{7,3}^{(3)hcp}$, A_{CH_4} , and ΔC_{CH_4} are the crystal sums of the hcp lattice, dipole-quadrupole polarizability, and quadrupole polarizability of methane, respectively.¹⁶ The experimental or theoretical values are $S_{7,3}^{(3)hcp} = 0.529i$ (where $i \equiv \sqrt{-1}$, [ref. 8]), $R_0 = 3.783 \text{ \AA}$ [ref. 8], $\Delta C_{CH_4}/A_{CH_4} = -0.52 \text{ \AA}$ [refs. 17, 18], and $\varepsilon_{3c}^{hcp} = -25.8 \text{ cm}^{-1}$ [ref. 8]. Thus, we arrive at an estimated value of $\varepsilon_4^{fcc} = -6.2 \text{ cm}^{-1}$.

The rovibrational states of methane in an fcc crystal are obtained by solving the standard vibration-rotation Hamiltonian matrix under the potential of Eq. (1). In figure 1 the rovibrational energy levels of methane and the optical selection rules are compared between the isolated molecule and the molecule in the fcc crystal. Those of the molecule in the hcp crystal are also shown in figure 1 for comparison. The solid arrows in the diagram for the isolated molecule and the molecule in the fcc crystal indicate allowed transitions. Since the space fixed components of the dipole moment belong to the $F_1 \overline{A}_2$ symmetry species in the extended group G^{fcc} , all

transitions become allowed for any orientation of polarization of light relative to the crystal axis. On the contrary, in the case of the hcp crystal, the parallel (solid arrows in figure 1) and perpendicular (dashed arrows) transitions show different selection rules since the hcp crystal *c*-axis is different from the other *a*- and *b*- axes.

The $J=1$ ground vibrational state belongs to $F_1\bar{F}_1$ symmetry in the extended group. Thus, the crystal field of O_h symmetry does not lift the degeneracy of the M -sublevels of $J=1$ as shown in figure 1. This is in contrast to the case of methane in the hcp crystal where the M -sublevels of $J=1$ split into two due to the crystal field of D_{3h} symmetry. In the same way, no splitting of the M -sublevels of $J=1$ is expected in the excited vibrational state in the fcc crystal.

The splitting caused by the crystal field of O_h symmetry first appears at $v=1, J=2, R=1$ levels having $F_1\bar{F}_2$ and $E\bar{F}_2$ symmetries. By the use of the crystal field value of $\varepsilon_4^{fcc} = -6.2 \text{ cm}^{-1}$, the splitting width of this level is numerically calculated to be $\sim 0.01 \text{ cm}^{-1}$.

Thus, for the infrared absorption spectrum of methane in the fcc crystal we expect only one absorption line for each rotational branch P(1), Q(1), and R(0), while the R(1) branch should appear as a doublet with a splitting of $\sim 0.01 \text{ cm}^{-1}$. These predictions are based on the assumption that the crystal structure is perfect. If there are some imperfection of the crystal stacking (as will be discussed later), the symmetry of the crystal field is further reduced, which may cause additional small splittings even in $J=1$ rotational levels.

III. EXPERIMENTAL

A. Kyoto University

Figure 2 shows a schematic of the experimental apparatus residing at Kyoto University

0.018, 0.020, and 0.024 cm^{-1} , respectively. The slightly broader width for the R(1) peak may reflect a contribution from the $\sim 0.01 \text{ cm}^{-1}$ crystal field induced splitting predicted above at the end of section II.B. The observation of only one absorption line for each rotational branch of $\text{CH}_4/\text{pH}_2(\text{fcc})$ indicates that the symmetry of the crystal field is almost perfectly O_h .

This set of four observed transitions is not sufficient to determine molecular parameters for $\text{CH}_4/\text{pH}_2(\text{fcc})$. All of these transitions satisfy a selection rule of $\Delta R = 0$ as is seen in figure 1. However, without $\Delta R \neq 0$ transitions, the rotational constant and the Coriolis parameter cannot be determined independently. Moreover, transitions to higher J levels are indispensable in determining the crystal field parameter ε_4^{fcc} quantitatively, since the crystal field potential is a function of only the fourth order Wigner's matrix. Prospective observations of Raman transitions, which obey a $\Delta J = 0, \pm 1$, and ± 2 selection rule, may allow us to determine molecular parameters for $\text{CH}_4/\text{pH}_2(\text{fcc})$.

Transitions of $\text{CH}_4/\text{pH}_2(\text{hcp})$ in figure 5 are clearly separated under high resolution, as predicted by theory.^{8,9} Especially noteworthy is a clearly resolved doublet at 1312.92 cm^{-1} and 1312.95 cm^{-1} which corresponds to the transitions $(J'=2, R'=1, M'=0, A_1 \overline{F}_2) \leftarrow (J'=1, M''=0 A_2 \overline{F}_1)$ and $(J'=2, R'=1, M'=\pm 1, E \overline{F}_1) \leftarrow (J'=1, M''=\pm 1, E \overline{F}_2)$, respectively (see Table III of Ref. 9). The high-resolution data in Table 2 allows us to modify the molecular parameters of $\text{CH}_4/\text{pH}_2(\text{hcp})$ in Ref. 9, which will be published separately along with those of all the isotopomers of methane.

We also observe small, but experimentally significant, differences in the transition frequencies between the rapid vapor deposited samples and the sample condensed in an enclosed cell, as is seen in figure 5 and Table II. These spectral differences are mainly explained by

C. Other Possible Microscopic Structures for Vapor Deposited pH₂ Solids

Although we have discussed the spectra obtained from rapid vapor deposited CH₄/pH₂ solids in terms of trapping of CH₄ molecules in hcp and fcc crystallites, it is important to consider whether other solid pH₂ structures might also be consistent with our data. The hcp and fcc structures are only two of the infinite number of densest close-packed structures derivable by stacking of close-packed planes.¹¹ The fcc structure (...ABCABCABC...) is actually the simplest in that each close-packed plane has the same translation relative to the plane below, whereas in hcp (...ABABAB...) each successive plane reverses its predecessor's lateral displacement.²⁰ Patterns with longer repeat units (polytypism), non-periodic structures such as twin and stacking faults, and even random stacked close-packed (rcp) structures are also possible, in principle.^{11, 20} However, if only nearest neighbor interactions are considered, then there are just two types of single substitutional trapping sites for any of these structures: sites in layers (B) embedded in regions of local hcp stacking (XABAX, "hcp-like"), or local fcc stacking (XABCX, "fcc-like").

We thus consider two extreme ideal structures for the transparent rapid vapor deposited pH₂ solids: (a) an aggregate of distinct perfect fcc and hcp crystallites in which ordered stacking sequences persist over dimensions larger than optical wavelengths, and (b) a random stacked close-packed solid for which fcc-like and hcp-like structures are intermingled at the molecular level. Without some independent knowledge of how CH₄ trapping site structures (and hence spectral perturbations) should differ in hcp vs. hcp-like pH₂ solids, we cannot make an unequivocal distinction based on the present spectroscopic data.

In an attempt to directly observe the effects of increasing structural disorder on the spectroscopy of CH₄/pH₂ solids, we performed a series of sample in vacuum depositions

employing successively slower pH₂ inlet flow rates. The slower flow rates result in lower deposition temperatures, which we hoped would further enhance the formation of metastable structures. The results are summarized in figure 6, which shows the Q(1) region of spectra of four as-deposited CH₄/pH₂ samples. Decreasing the pH₂ inlet flow from 190 to 45 mmol/h, traces (6a) and (6b), indeed results in increased intensity for CH₄/pH₂(fcc) absorptions, in slightly broader linewidths, and in slightly improved alignment of the hcp c-axes with the substrate surface normal. However, further decreasing the pH₂ inlet flow to 10 and then to 4 mmol/h, traces (6c) and (6d), results in relatively weaker CH₄/pH₂(fcc) absorptions and in narrower lines; the trend towards increased alignment between hcp c-axes and the substrate surface normal is continued. Surprisingly, all of these samples exhibited excellent optical transparency, even the two deposited at the slowest flow rates.

Absent a qualitative spectroscopic signature for the formation of a microscopically disordered random close packed solid, we conclude that the mixed hcp/fcc crystallite model is capable of explaining all of our results to date. We await the application of theoretical techniques such as quantum Monte Carlo simulations of trapping site structures in imperfect crystals, and the accumulation of a broader spectroscopic database on doped pH₂ solids to definititively resolve this issue.

V. CONCLUSIONS

Two methods for preparing millimeters thick, optically transparent, doped pH₂ solids have been presented: gas condensation in an enclosed cell, and rapid vapor deposition onto a substrate in vacuum. Rapid vapor deposition of precooled pH₂ gas onto a ≈ 2 K substrate in

TABLES

TABLE I. Symmetry adapted rotational wavefunctions of the ground vibrational state expressed as linear combinations of the symmetric top rotational wavefunction $|kJm\rangle$ and their representation in the extended group G .

$J=0$	$A_1 \overline{A_1}$	$ 0,0,0\rangle$
$J=1$	$F_1 \overline{F_1}$	$ 0,1,0\rangle, \pm 1,1,0\rangle, 0,1,\pm 1\rangle, \pm 1,1,-1\rangle, \pm 1,1,1\rangle$
$J=2$	$E \overline{E}$	$\frac{1}{2} [-2,2,-2\rangle + 2,2,-2\rangle + -2,2,2\rangle + 2,2,2\rangle], \frac{1}{\sqrt{2}} [0,2,-2\rangle + 0,2,2\rangle],$ $\frac{1}{\sqrt{2}} [-2,2,0\rangle + 2,2,0\rangle], 0,2,0\rangle$
	$E \overline{F_2}$	$\frac{1}{2} [-2,2,-2\rangle - 2,2,-2\rangle + -2,2,2\rangle - 2,2,2\rangle], \frac{1}{\sqrt{2}} [-2,2,0\rangle - 2,2,0\rangle],$ $ \pm 1,2,0\rangle, \pm 1,2,2\rangle$
	$F_2 \overline{E}$	$\frac{1}{2} [-2,2,-2\rangle + 2,2,-2\rangle - -2,2,2\rangle - 2,2,2\rangle], \frac{1}{\sqrt{2}} [0,2,-2\rangle - 0,2,2\rangle],$ $\frac{1}{\sqrt{2}} [-2,2,\pm 1\rangle + 2,2,\pm 1\rangle], 0,2,\pm 1\rangle$
	$F_2 \overline{F_2}$	$\frac{1}{2} [-2,2,-2\rangle - 2,2,-2\rangle - -2,2,2\rangle + 2,2,2\rangle], \frac{1}{\sqrt{2}} [\pm 1,2,-2\rangle - \pm 1,2,2\rangle],$ $\frac{1}{\sqrt{2}} [-2,2,\pm 1\rangle - 2,2,\pm 1\rangle], \pm 1,2,-1\rangle, \pm 1,2,1\rangle$

TABLE II. Absorption peaks (cm^{-1}), and spectroscopic assignments for ν_4 fundamental band of CH_4/pH_2 . The labels (5a), (5b), and (5c) refer to the spectral traces and sample descriptions in figure 5.

(5a)	(5b)	(5c)	assignment	$(J', R', M', \Gamma') \leftarrow (J'', M'', \Gamma'')$
1298.236	1298.240	1298.237	P(1) hcp \parallel	$(0,1,0, A_1 \bar{F}_2) \leftarrow (1,0, A_2 \bar{F}_1)$
1298.312			P(1) fcc	$(0,1,x, A_1 \bar{F}_2) \leftarrow (1,x, F_1 \bar{F}_1)$
1298.892	1298.898	1298.894	P(1) hcp \perp	$(0,1,0, A_1 \bar{F}_2) \leftarrow (1,\pm 1, E \bar{F}_2)$
1302.943	1302.943	1302.944	Q(1) hcp \perp	$(1,1,\pm 1, E \bar{F}_1) \leftarrow (1,0, A_2 \bar{F}_1)$
1303.331	1303.332		Q(1) fcc	$(1,1,x, F_1 \bar{F}_2) \leftarrow (1,x, F_1 \bar{F}_1)$
1303.598	1303.600	1303.600	Q(1) hcp \parallel	$(1,1,\pm 1, E \bar{F}_1) \leftarrow (1,\pm 1, E \bar{F}_2)$
1303.846	1303.849	1303.848	Q(1) hcp \perp	$(1,1,0, A_2 \bar{F}_2) \leftarrow (1,\pm 1, E \bar{F}_2)$
1308.259	1308.255	1308.261	R(0) hcp \perp	$(1,0,0, E \bar{A}_1) \leftarrow (0,0, A_1 \bar{A}_1)$
1308.377	1308.374	1308.376	R(0) hcp \parallel	$(1,0,\pm 1, A_2 \bar{A}_2) \leftarrow (0,0, A_1 \bar{A}_1)$
1308.412	1308.412		R(0) fcc	$(1,0,x, F_1 \bar{A}_2) \leftarrow (0,x, A_1 \bar{A}_1)$
1309.188	1309.185	1309.191	R(0) hcp \perp	$(1,2,\pm 1, E \bar{F}_2) \leftarrow (1,\pm 1, E \bar{F}_2)$
1312.289	1312.290	1312.292	R(1) hcp \perp	$(2,1,\pm 1, E \bar{F}_1) \leftarrow (1,0, A_2 \bar{F}_1)$
1312.92 sh	1312.93 sh	1312.923	R(1) hcp \parallel	$(2,1,0, A_1 \bar{F}_2) \leftarrow (1,0, A_2 \bar{F}_1)$
1312.960	1312.945	1312.947	R(1) hcp \parallel	$(2,1,\pm 1, E \bar{F}_1) \leftarrow (1,\pm 1, E \bar{F}_2)$
1313.054			R(1) fcc	$(2,1,0, E \bar{F}_2) \leftarrow (1,x, F_1 \bar{F}_1)$
			R(1) fcc	$(2,1,\pm 1, F_1 \bar{F}_2) \leftarrow (1,x, F_1 \bar{F}_1)$
1313.578	1313.579	1313.578	R(1) hcp \perp	$(2,1,0, A_1 \bar{F}_2) \leftarrow (1,\pm 1, E \bar{F}_2)$
1316.504	1316.515	1316.510	R(1) hcp \perp	$(2,1,\pm 2, E \bar{F}_2) \leftarrow (1,\pm 1, E \bar{F}_2)$

\parallel and \perp - polarizations relative to c-axis in hcp pH₂

x - all M substates remain degenerate

sh - shoulder

FIGURE CAPTIONS

FIG. 1. Rotational levels of the ground and v_4 excited vibrational states of: (1) isolated CH_4 , (2) CH_4 in fcc pH₂, and (3) CH_4 in hcp pH₂. Allowed transitions are shown as vertical solid arrows in the diagram of *isolated* and *fcc*. Vertical solid and dashed arrows in the diagram of *hcp* shows the parallel and perpendicular transitions, respectively. The irreducible representation of each rotational level in terms of the extended group G is listed at the right-hand-side of the energy levels in each diagram.

FIG. 2. Experimental schematic (Kyoto University).

FIG. 3. Experimental schematic (Edwards Air Force Base).

FIG. 4. Overview of the v_4 region in IR absorption spectra of a rapid vapor deposited CH_4/pH_2 sample. Trace (a) is for the as-deposited sample at $T_{\text{sub}} = 2.2$ K, (b) warmed to $T_{\text{sub}} = 4.4$ K, (c) cooled to $T_{\text{sub}} = 3.0$ K, and (d) shows the annealed sample cooled to $T_{\text{sub}} = 2.2$ K. The sample remains at each temperature for 1 h as 200 interferometer scans (0.1 cm^{-1} resolution) are accumulated. During the 25 minute long deposition the pH₂ inlet rate is 190 mmol/h (sample thickness growth rate = 50 $\mu\text{m}/\text{min}$) and T_{sub} rises from 2.2 to 3.2 K. The final CH_4 concentration is estimated as 110 PPM, and the sample thickness as 1.2 mm. Most peaks show instrument limited linewidths of $\approx 0.1 \text{ cm}^{-1}$. The peaks in trace (a) which dramatically decrease in intensity upon annealing are marked with asterisks.

FIG. 5 High resolution detail of the ν_4 absorption region of CH_4/pH_2 samples produced by rapid vapor deposition, and by gas condensation in an enclosed cell. Trace (a) shows the rapid vapor deposited sample at $T_{\text{sub}} = 2.4$ K immediately after deposition. Trace (b) shows the rapid vapor deposited sample at $T_{\text{sub}} = 4.5$ K, after a double annealing cycle: $2.4 \text{ K} \rightarrow 4.8 \text{ K} \rightarrow 3.6 \text{ K} \rightarrow 2.4 \text{ K} \rightarrow 4.5 \text{ K}$. The sample remains at each temperature for 1 h as 40 interferometer scans (0.008 cm^{-1} resolution) are accumulated. During the 1 h long rapid vapor deposition the pH_2 inlet rate is 190 mmol/h (sample thickness growth rate = $50 \mu\text{m}/\text{min}$) and T_{sub} rises from 2.2 to 3.2 K. The final CH_4 concentration is estimated as 15 PPM, and the sample thickness as 2.9 mm. The peaks in trace (a) which dramatically decrease in intensity upon annealing are marked with asterisks. Trace (c) shows a spectrum (0.01 cm^{-1} resolution) of the enclosed cell condensed sample cooled to 4.5 K following the 2 h long sample growth process at $T \approx 8$ K; the isolated CH_4 concentration is estimated as 2 PPM. The symbols \parallel and \perp indicate the predicted polarizations, relative to the hcp crystal c-axis, for allowed transitions of CH_4 molecules trapped in hcp pH_2 .

FIG. 6 High resolution spectra (0.005 cm^{-1} resolution) of the Q(1) feature for as-deposited CH_4/pH_2 samples produced at various pH_2 flow rates. Details for each 1 h long deposition: (a) pH_2 inlet rate is 190 mmol/h, T_{sub} rises from 2.2 to 3.2 K, final sample thickness $d = 2.9 \text{ mm}$, and the CH_4 concentration $C_{\text{CH}_4} \approx 15 \text{ PPM}$, (b) pH_2 inlet rate = 45 mmol/h, T_{sub} rises from 2.2 to 2.4 K, $d = 0.8 \text{ mm}$, and $C_{\text{CH}_4} \approx 55 \text{ PPM}$, (c) pH_2 inlet rate is 10 mmol/h, T_{sub} rises from 2.2 to 2.3 K, $d = 0.2 \text{ mm}$, and $C_{\text{CH}_4} \approx 200 \text{ PPM}$, and (d) pH_2 inlet rate is 4 mmol/h, T_{sub} remains at 2.2 K, $d = 0.08 \text{ mm}$, and $C_{\text{CH}_4} \approx 550 \text{ PPM}$. The symbols $*$, \parallel , and \perp are defined in the captions to figures 4 and 5.

REFERENCES

1. T. Oka, *Annu. Rev. Phys. Chem.* **44**, 299 (1993).
2. T. Momose, M. Miki, M. Uchida, T. Shimizu, I. Yoshizawa, and T. Shida, *J. Chem. Phys.* **103**, 1400 (1995).
3. T. Momose and T. Shida, *Bull. Chem. Soc. Jpn.* **71**, 1 (1998).
4. H. Hoshina, T. Wakabayashi, T. Momose, and T. Shida, *J. Chem. Phys.* **110**, 5728 (1999).
5. M.E. Fajardo and S. Tam, *J. Chem. Phys.* **108**, 4237 (1998).
6. S. Tam and M.E. Fajardo, *Rev. Sci. Instrum.* **70**, 1926 (1999).
7. G.W. Collins, W.G. Unites, E.R. Mapoles, and T.P. Bernat, *Phys. Rev. B* **53**, 102 (1996).
8. T. Momose, *J. Chem. Phys.* **107**, 7695 (1997).
9. T. Momose, M. Miki, T. Wakabayashi, T. Shida, M.C. Chan, S.S. Lee, and T. Oka, *J. Chem. Phys.* **107**, 7707 (1997).
10. T. Momose, H. Katsuki, H. Hoshina, N. Sogoshi, T. Wakabayashi, and T. Shida, *J. Chem. Phys.* **107**, 7717 (1997)
11. C. Kittel, Introduction to Solid State Physics 6th Edition, (Wiley, New York, 1986).
12. R. E. Miller, and J. C. Decius, *J. Chem. Phys.* **59**, 4871 (1973).
13. H. F. King, and D. F. Horning, *J. Chem. Phys.* **44**, 4520 (1966).
14. E. P. Wigner, *Group Theory* (Academic Press, New York, 1959).
15. T. Momose, manuscript in preparation.
16. A. D. Buckingham, *Adv. Chem. Phys.* **12**, 107 (1967).
17. G. Maroulis, *Chem. Phys. Lett.* **226**, 420 (1994).

Figure 2

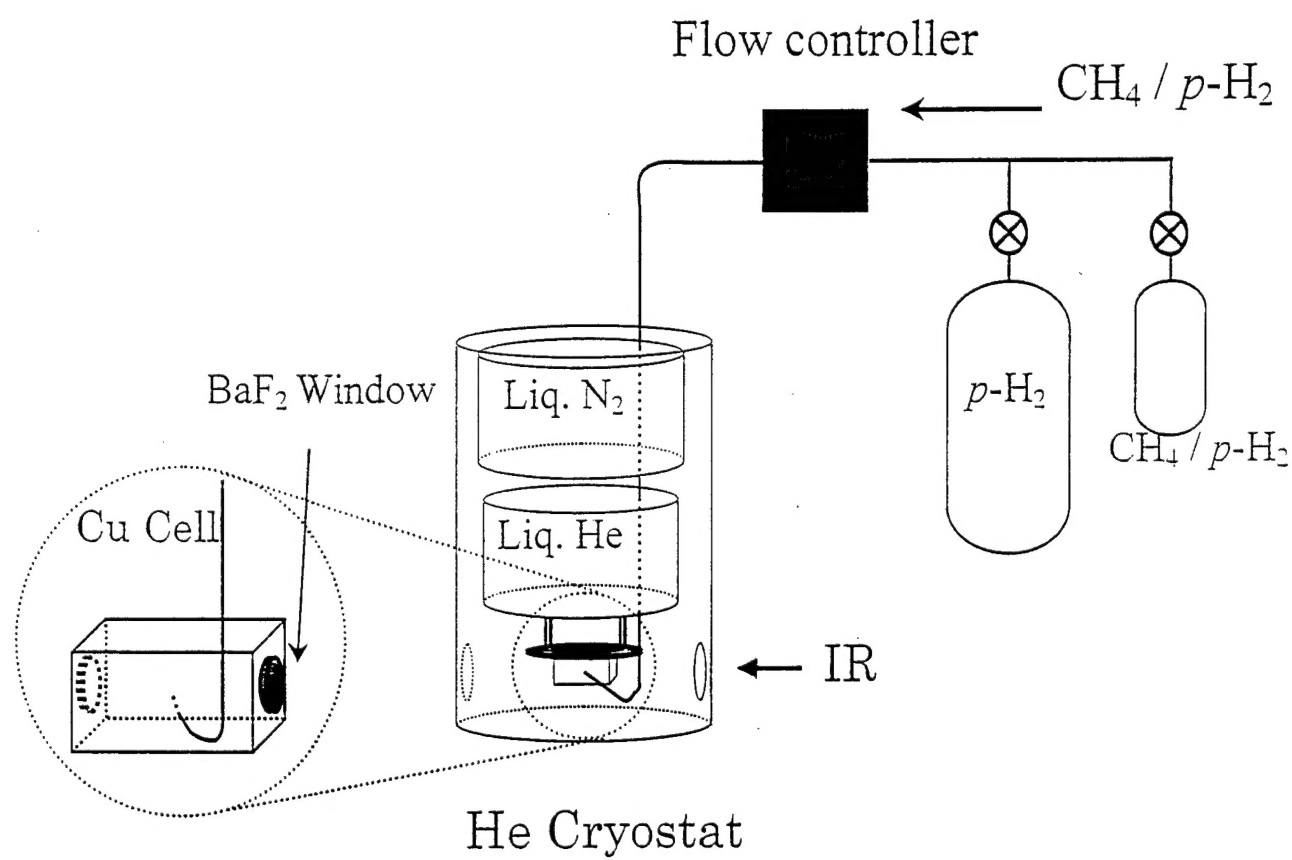


Figure 3

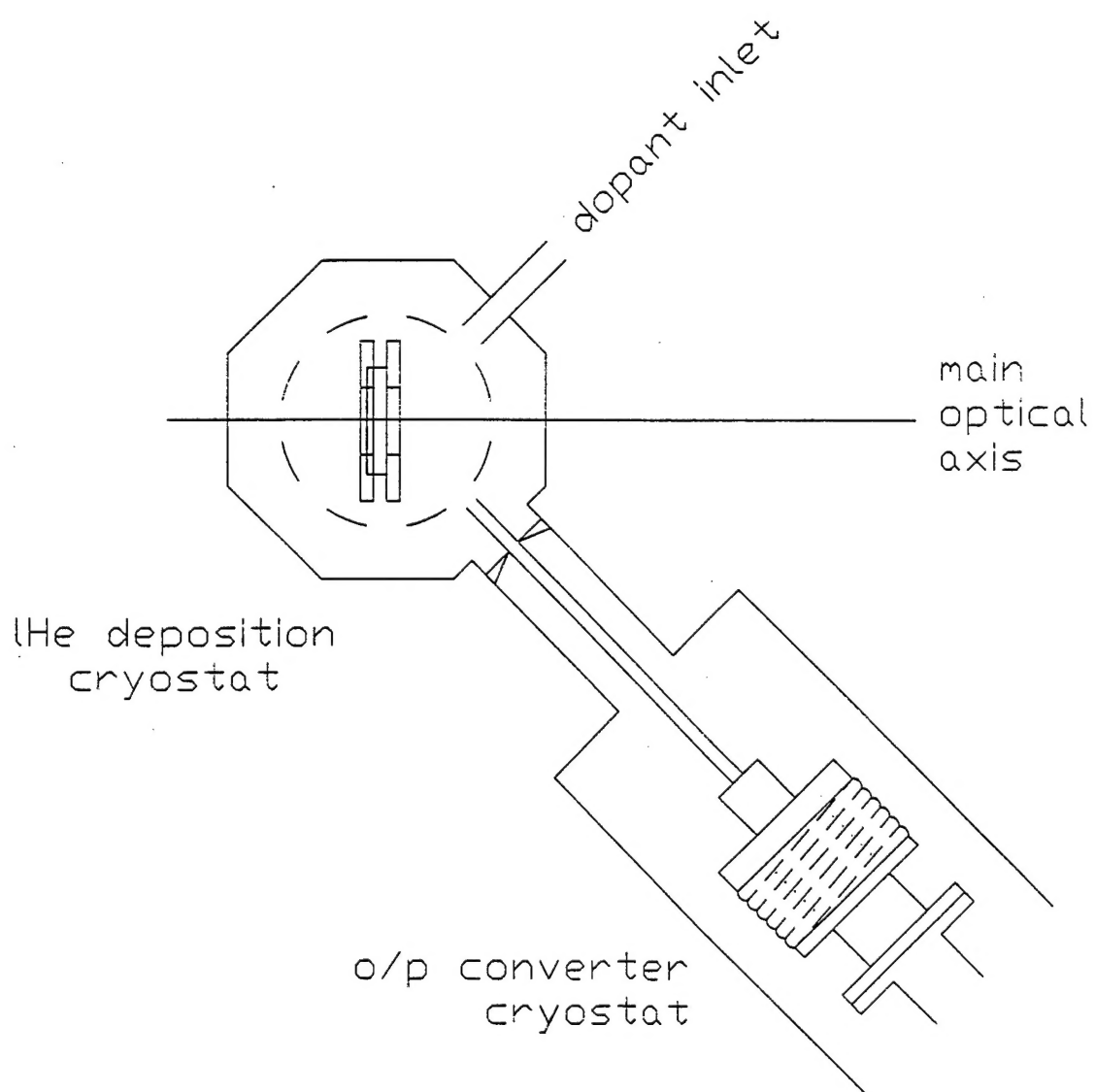


Figure 5

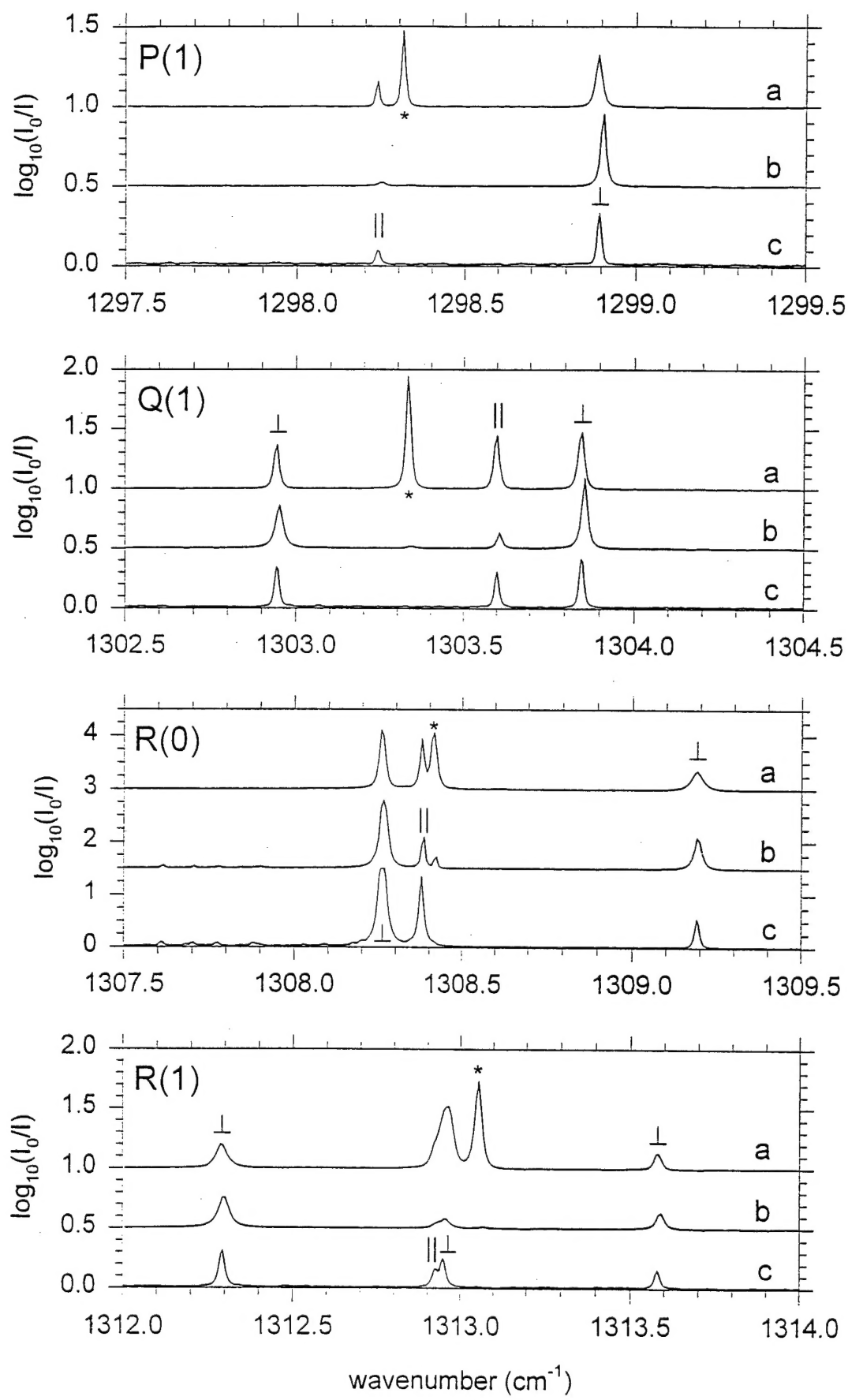


Figure 6

